arXiv:0709.0468v1 [nucl-ex] 4 Sep 2007

High-j single-particle neutron states outside the N=82 core

B.P. Kay,[1] S.J. Freeman,[1,*] J.P. Schiffer,[2] J.A. Clark,[3]
C. Deibel,[3] A. Heinz,[3] A. Parikh,[3,†] and C. Wrede[3]

[1]*Schuster Laboratory, University of Manchester, Manchester M13 9PL, UK*
[2]*Argonne National Laboratory, Argonne, Illinois 60439, USA*
[3]*A.W.Wright Nuclear Structure Laboratory,*
Yale University, New Haven, Connecticut 06520, USA

(Dated: February 1, 2008)

Abstract

The behaviour of the $i_{13/2}$ and $h_{9/2}$ single-neutron strength was studied with the (α,^{3}He) reaction on ^{138}Ba, ^{140}Ce, ^{142}Nd and ^{144}Sm targets at a beam energy of 51 MeV. The separation between the single-neutron states $i_{13/2}$ and $h_{9/2}$ was measured in N=83 nuclei with changing proton number. To this end spectroscopic factors for states populated in high-ℓ transfer were extracted from the data. Some mixing of ℓ=5 and 6 strength was observed with states that are formed by coupling the $f_{7/2}$ state to the 2^+ and 3^- vibrational states and the mixing matrix elements were found to be remarkably constant. The centroids of the strength indicate a systematic change in the energies of the $i_{13/2}$ and $h_{9/2}$ single-neutron states with increasing proton number that is in quantitative agreement with the effects expected from the tensor interaction.

PACS numbers: 21.10.Jx, 25.55.Hp, 27.60.+j

---

[*] Correspondence to: sean.freeman@manchester.ac.uk

[†] Current address: Departament de Fisica i Enginyeria Nuclear, Universitat Politecnica de Catalunya, E-08036, Barcelona, Spain

The description of nuclear structure in terms of single nucleons moving within the nuclear mean field is at the root of much of the understanding of atomic nuclei. The properties of the available single-particle orbitals close to the Fermi surface are essential ingredients in the understanding of many phenomena, from the description of nuclear excitations within a shell model to the development of collectivity in low-lying vibrational states. There is increasing experimental evidence, emerging in situations where shell structure can be tracked across a range of neutron excess, that the sequence of single-particle states is not static and can change with neutron-to-proton ratio, indeed changing the 'closed shells' in some regions of lighter nuclei that are far from stability. For example, changes in single-particle states occurring in neutron-rich oxygen isotopes have been observed that destroy the familiar magic gap at $N = 20$ close to the neutron dripline, whilst producing a new one at $N = 16$ [1]. In heavier nuclei, systematic shifts in energies of single-particle states have been observed, indicating similar evolution of shell structure with changing neutron excess [2].

Recently, Otsuka and co-workers identified the tensor part of the nucleon-nucleon interaction as a general feature that appears to drive these observed trends in the evolution of nuclear shell structure in different mass regions [3]. This is an interesting finding since, beyond the quadrupole moment of the deuteron, there have been only a few instances where this inherent component of the nucleon-nucleon force manifests itself in nuclear structure in an obvious fashion [4]. The tensor component of the nucleon-nucleon interaction has now been shown to have a systematic effect on single-particle energies, an effect that can even cause the making and breaking of magic numbers [3]. Efforts are now underway to include tensor components into Hartree-Fock (HF) mean-field models where they had been largely neglected [5, 6, 7].

Care needs to be taken when comparing theoretical predictions of single-particle energies with experimental data. Often little is known about the single-particle nature of the states in question. The energy of the lowest state of a given spin-parity can give misleading estimates for the energy of the corresponding single-particle orbital if there is significant fragmentation of strength. Nucleon transfer reactions are a good probe of such fragmentation. However, even if experimental spectroscopic factors have been determined using such methods, their absolute values are often of questionable meaning as they depend quite sensitively on choices made in the calculation of reaction cross sections. For example, small changes in the bound-state radius of the transferred particle, or differences in optical-model potentials, can have a dramatic effect on the magnitude of the calculated cross sections without appreciably changing the predicted angular distributions. The comparison of isolated experiments on different targets can therefore be fraught with difficulty arising from the details of the reaction models employed, in addition to any systematic experimental differences. Careful studies across all targets of interest, using the same experimental methods and the same choices in the extraction of spectroscopic factors, can alleviate most of these difficulties, at least in obtaining good relative spectroscopic factors. The kinematic characteristics of a particular transfer reaction also influence the reliability of spectroscopic factors. The assumptions inherent in the reaction models are best met where there is good momentum matching, ensuring relatively large cross sections for the direct transfer process. Many studies have been performed on reactions, such as (d,p), which are well matched for low-ℓ transfer. However, there are fewer systematic studies where there is a large reaction Q value, and consequently higher momentum transfer, leading to large cross sections for direct high-ℓ transfers. Such reactions are therefore needed for reliable measurements of high-j orbitals.

The work reported in Ref. [2] describes the use of the (α,t) reaction on stable tin targets to populate high-j single-proton states in Sb isotopes. The relative spectroscopic factors for ℓ=4 and 5 transfer were extracted using the same parameters in distorted-wave Born approximation (DWBA) calculations and a common normalisation factor. The results identifed the lowest $11/2^-$ and $7/2^+$ states with the dominant fragment of $h_{11/2}$ and $g_{7/2}$ single-proton states, with strengths constant to within ±10%. No single potential could describe the energetic separation of these states as a function of neutron number until the introduction of a tensor term in the residual interaction [3, 5]. The variation of the lowest known experimental states with the requisite spin and parity points to the possibility of a similar evolution of single-particle energies for neutrons outside N=82 [2], in particular, for the $\nu i_{13/2}$ and $\nu h_{9/2}$ orbitals. However, the single-particle nature of the states involved is somewhat uncertain as no previous study of had been undertaken using reactions that are well matched for high-ℓ transfers.

Here we present a systematic study of spectroscopic factors across the stable metallic N=82 isotopes using the (α,^{3}He) reaction, which has good kinematic matching for $\ell \sim 6$. We have identified states populated with high-ℓ transfer and extracted relative spectroscopic strengths for ℓ=5 and 6, allowing the centroids of $i_{13/2}$ and $h_{9/2}$ strength to be determined.

Since these states have no radial nodes, the comparison of their relative energies is largely insensitive to anything other than specific features of the residual interaction, as was the case for the states in Sb isotopes studied earlier.

A beam of α particles with an energy of 51 MeV was supplied by the Yale tandem Van de Graaff accelerator and was used to bombard targets of ^{138}Ba, ^{140}Ce, ^{142}Nd and ^{144}Sm. Oxygen is an almost inevitable contaminant in such targets due to their chemical reactivity. To avoid complex handling procedures associated with self-supporting metallic targets, material was evaporated from enriched oxides onto supporting carbon foils of thickness 20–40 μg cm^{-2}, which were then stored in an argon atmosphere with only brief exposure to air. Reactions on both oxygen and the carbon backing complicated the analysis, as discussed in detail below. The Yale Enge split-pole spectrometer was used to momentum analyse the products from the reactions. A gas-filled ionisation chamber and plastic scintillator, at the focal plane of the spectrometer, were used to isolate ^{3}He ions from other reaction products on the basis of their energies and energy-loss characteristics. A Si monitor detector was placed in the target chamber at 30° for diagnostic purposes. The beam dose was measured using a Faraday cup and beam-current integrator. The beam currents were typically in the range 10-30 pnA. Data were collected using the same experimental set-up in two separate experimental runs.

In order to extract absolute cross sections, the product of the target thickness and spectrometer aperture was calibrated using elastic scattering at low beam energies. In the first run this was done with a spectrometer angle of 30° at an incident energy of 10 MeV. In the second run, elastic scattering of 20-MeV α particles was measured at 20°. The deviation from Rutherford scattering under both of these conditions is predicted to be less than 0.5% in calculations using several different optical-model parameters. The entrance aperture of the spectrometer was kept constant throughout each run to avoid any systematic differences. Using the nominal value of the entrance aperture, the ^{138}Ba, ^{140}Ce and ^{142}Nd targets were found to be in the range 100-150 μg cm^{-2}; the ^{144}Sm target was thinner at $\sim$40 μg cm^{-2}. No significant variation in the normalisation from yield to cross section was observed between measurements made at the beginning and end of each run, and between the two runs, showing that the targets are fairly robust.

Typical momentum spectra for the observed ions are shown in Fig. 1, where the main N=82 reaction strengths are via ℓ=5 and 6 transfer, with the exception of some ℓ=3 transitions leading to the $7/2^-$ ground state of the residual nucleus. An energy resolution of ~70 keV was obtained. Both ℓ=5 and ℓ=6 strengths are split into two groups in each isotope. Also apparent in the spectra are intense lines arising from reactions on ^{16}O and ^{12}C target contaminants. These contaminant peaks obscure some of the lines of interest at certain angles. However, the kinematic characteristics are such that the momenta of the ions from contaminants change more quickly with angle than for the reactions on N=82 targets, allowing angles to be found where each peak of interest is free from contamination. Weaker contaminant transitions from ^{28}Si(α,^{3}He) reactions were also present in some spectra, particularly those from the ^{144}Sm target. They were easily identified using known excitation energies and from the momentum variation with angle and were not close to any peaks of interest.

Data were taken at laboratory angles of 6°, 11° and 20° for all targets. The first angle was chosen to be as close to the peak yields for ℓ=5 and 6 as possible without resulting in count-rate problems, whilst 11° and 20° are angles sensitive to the differences in the shapes of angular distributions. For the ^{138}Ba target, where contaminant ion groups cause most problems, spectra were also taken at 30°. Since spectroscopic factors are most reliable when measured at the peak of the angular distribution at forward angles, measurements were also made at 30° using the ^{140}Ce target as a consistency check on the reliability of spectroscopic factors obtained at the larger angles.

Examples of angular distributions are shown in Fig. 2, together with DWBA calculations using optical-model and bound-state parameters listed in Table I. The optical potentials were successful in reproducing angular distributions of high-ℓ transitions in Sn(α,t) reactions [2]. The exact finite-range calculations were performed using the computer code PTOLEMY [12]. The comparison with data indicates the quality of the DWBA calculations in reproducing the angular variation in cross section. Spin assignments were taken from the literature [13, 14, 15, 16] although, in general, the measured angular distributions agree with these spin assignments on the assumption that ℓ=5 and 6 transitions lead to the population of $9/2^-$ and $13/2^+$ states, respectively. No strong transitions were observed with transfers other than ℓ=3, 5 and 6.

In ^{141}Ce there is a doublet composed of a $13/2^+$ state at 1354.52(9) keV and a $9/2^-$ state at 1368.7(2) keV [14] that are unresolved in the momentum spectra. Yields for these two states were extracted by fitting two Gaussian functions to the data with positions fixed using the known excitation energies. The widths were fixed to values reproducing the shape of neighbouring singlet peaks, such that the peak heights were the only free parameter in the fit. This procedure was successful at 20° and 30°. At 6° and 11° satisfactory fits were not obtained due to an increasing background in the spectra from inelastically scattered α particles that cannot be completely separated from ejectile ^{3}He ions at forward angles. An alternative method, fitting two calculated ℓ=5 and 6 angular distributions to the summed yield of the doublet led to ambiguous results, with a long flat trough in the χ^2 space, due to the similarity in shape of the two distributions.

Table II gives the differential cross sections measured in the current work, where absolute numbers typically have an error of $\sim$ 7% whilst relative numbers are good to 5%. Where a cross section value is not listed in the table, that particular angle was affected by contamination by oxygen or carbon ion groups. In addition, data were not taken at 30° for ^{142}Nd and ^{144}Sm targets and yields could not be extracted from the ^{141}Ce doublet at forward angles, as discussed above. Also shown are the spectroscopic factors obtained using a single normalisation for both $\ell = 5$ and 6 transfers across all isotopes and transitions listed. The spectroscopic factors at different angles typically varied by less than 10% from the average values listed in Table II, apart from those arising from the Ce doublet peak where the observed variation was less than the larger errors arising from the fitting procedure. The relative values of the spectroscopic factors are subject to an uncertainty of $\sim$ 10%, based on the error in the relative cross sections and analyses performed using a variety of different sets of optical-model parameters. Spectroscopic factors were not extracted for the $\ell = 3$ transitions to the residual ground states; DWBA calculations were not able to reliably predict the shape of these poorly-matched transfers. The spectroscopic factors show significant deviations from those extracted previously using (d,p) reactions ([13, 14, 15, 16] and references therein), not only between different targets, but even for a given target with the same ℓ-value, as might be expected when comparing spectroscopic strengths extracted from poorly-matched and well-matched transitions. The totals for ℓ =5 and for 6 strengths, shown in Table III, are constant to within ±13% across the isotopes studied.

High-ℓ transfers populate two states for both $\ell = 5$ and 6 in each final nucleus; no other transitions were observed with these ℓ transfers to a limit of 5% of the strongest transition. This fragmentation is likely to be due to coupling to vibrational excitations of the core, leading to predominately two-state mixing between $0^+_{\rm core} \otimes \nu i_{13/2}$ and $3^-_{\rm core} \otimes \nu f_{7/2}$

configurations in the case of the positive-parity states, and $0^+_{\mathrm{core}} \otimes \nu h_{9/2}$ and $2^+_{\mathrm{core}} \otimes \nu f_{7/2}$ configurations for the negative-parity states. Simple two-level mixing calculations have been used to extract the mixing matrix elements from the measured spectroscopic factors and excitation energies. The values of the matrix elements are shown in Table III. They are remarkably constant across all the nuclei studied, leaving the extent of the mixing to be dictated by the energetic proximity of the unperturbed states, illustrated in Fig. 3 (a) and (b). More detailed calculations with particle-core coupling models have been done in the past, where parameters were fitted to the available energies and spectroscopic factors [17, 18, 19, 20]. The results of these calculations are broadly in line with the experimental results of the current work, although they have been fitted to spectroscopic factors from (d,p) reactions so a detailed comparison is not appropriate here.

The trend in the $i_{13/2}$ and $h_{9/2}$ centroids is similar to that of the lowest $9/2^-$ and $13/2^+$ states, as illustrated by the energy differences shown in Fig 3(c). However, the fall in energy with increasing Z is not as large and the crossing of the two lowest states is not observed in the single-particle energies.

In the Z=51 isotopes, the observed evolution of the $\pi h_{11/2} - \pi g_{7/2}$ gap as a function of neutron number, which is somewhat similar to the trends uncovered here, has been successfully reproduced by the introduction of the tensor-force terms in shell-model and mean-field calculations [3, 5]. Qualitatively, these shifts have a fairly simple effect: nucleons filling a $j = \ell \pm s$ orbit have an attractive effect with nucleons in $j = \ell \mp s$ orbitals, whereas a repulsive contribution to binding energy arises from the interaction between nucleons where both are either in $j = \ell + s$ or $j = \ell - s$ states [3].

In the case of neutron states outside the N=82 core, the tensor force will also produce such a shift arising from changes in the occupancy of various proton orbits. Experimental proton occupancies in N=82 nuclei are available from previous systematic measurements of proton-transfer reactions [21]; over the stable isotopes, the $\pi 1g_{7/2}$ and $\pi 2d_{5/2}$ orbits were observed to fill at approximately the same rate. These proton orbitals have opposite effects on neutron binding energies, having different spin-orbit couplings, $j = \ell - s$ and $j = \ell + s$. But the effect of the $\pi 1g_{7/2}$ state should dominate, due to the considerably larger spatial overlap with the nodeless radial wavefunctions of the high-j neutron states. An increased binding energy for $i_{13/2}$ neutrons, and a decrease for $h_{9/2}$, should therefore result from a tensor interaction with $g_{7/2}$ protons. As the occupancy of this proton orbital increases, the two neutron states should drift towards each other in energy. This qualitative expectation is in agreement with the current experimental results, as illustrated in Fig. 3. More quantitatively, the effect of a tensor force based on π and ρ meson potential (discussed in detail in Ref. [3]) is to reduce the difference between $i_{13/2}$ and $h_{9/2}$ neutrons by 0.180 MeV per additional proton in the $\pi g_{7/2}$ orbital, using calculations of the relevant matrix elements using A=140 harmonic oscillator wave functions [22]. In line with the qualitative expectations discussed above, the interaction with a $\pi d_{5/2}$ proton is calculated to increase the gap by only 0.04 MeV. Combining these tensor matrix elements with measured proton occupancies [21], the relative changes produced by the tensor interaction on the $\nu i_{13/2} - \nu h_{9/2}$ gap can be deduced. A comparison of this calculation with the experimental single-particle energy differences is shown in Fig. 3(d), displaying reasonable agreement with the measured changes to the $\nu i_{13/2} - \nu h_{9/2}$ gap.

Calculations with mean-field models are more difficult in this case, compared to the situation with proton orbitals outside Z=50, due to the need to reproduce the details of the filling of protons in the close-lying $\pi g_{7/2}$ and $\pi d_{5/2}$ orbitals near the Fermi surface. These states are known experimentally to lie only ∼100-300 keV apart [21]. Recently HF plus BCS calculations have been published for neutron states outside N=82 [7], based on a modification to the SLy5 Skyrme interaction that introduces elements from the tensor force. It predicts a different pattern of filling proton orbitals compared to that deduced experimentally, namely sequential filling of the $\pi g_{7/2}$ level, followed by the $\pi d_{5/2}$ orbital. As a result, there are discrepancies between the calculated changes to the $\nu i_{13/2} - \nu h_{9/2}$ gap as a function of Z and the experimental data presented here.

No quantitative information exists on the single-neutron nature of high-j states in N=83 nuclei, other than those accessible in neutron-adding reactions on the stable metallic species. There are no $13/2^+$ states known in ^{137} Xe; measurements in normal kinematics for a ^{136}Xe gas target are compromised by reactions on gas-cell windows leading to contamination problems. In lighter N=83 nuclides, direct experimental information about low-lying $13/2^+$ states is missing. However, the energies of both the *lowest* $13/2^+$ and $9/2^-$ states are known for $Z > 62$, even though spectroscopic factors are unavailable. Beyond $Z = 62$ there is a sudden change in the energy systematics; the two states start to diverge in energy quite strongly (see Fig. 3(c)). In these higher Z systems, the $\pi h_{11/2}$ state should begin to fill, with dramatic consequences for high-j neutron states due to their large radial overlap and an increasing repulsive contribution from a tensor interaction, amounting to 0.16 MeV per additional proton [22]. However, any strong conclusions should be treated with some caution since the single-particle content of the lowest-lying states will not be known until nucleon-adding reactions are performed on radioactive beams. Indeed, it is towards the Z=64 sub-shell closure that the 3^- core excitation is expected to fall closest in energy to the centroid of $i_{13/2}$ strength (see Fig. 3(b)). Assuming the mixing matrix elements are of similar strength to those extracted here, this will lead to large mixing and significant fragmentation of ℓ=6 strength between two $13/2^+$ states. The energy of the lowest $13/2^+$ state will therefore be a particularly unreliable estimate of the $i_{13/2}$ single-neutron energy.

In conclusion, spectroscopic factors have been measured for high-j states outside stable N=82 isotopes revealing a systematic drift in $i_{13/2}$ and $h_{9/2}$ single-neutron energies toward each other with increasing proton number. There is quantitative agreement between the experimental trends and the shifts in single-particle energies predicted with a tensor interaction.

We are indebted to Takaharu Otsuka for providing us with the relevant tensor matrix elements and for many very fruitful discussions. We would like to acknowledge meticulous target manufacture by John Greene (Argonne National Laboratory) and Paul Morrall (Daresbury Laboratory). Peter Parker has provided invaluable assistance and advice, without which these measurements would not have been possible. We would also like to thank the staff at Yale University, in particular, their efficient facility operation. This work was supported by the UK Science and Technology Facilities Council and the US Department of Energy, Office of Nuclear Physics, under Contract Numbers DE-FG02-91ER-40609 and DE-AC02-06CH11357.

---

[1] A. Ozawa, T. Kobayashi, T. Suzuki, K. Yoshida and I. Tanihata, Phys. Rev. Lett. 84, 5493 (2000).

[2] J.P. Schiffer, S.J. Freeman, J.A. Caggiano, C. Deibel, A. Heinz, C.-L. Jiang, R. Lewis, A. Parikh, P.D. Parker, K.E. Rehm, S. Sinha and J.S. Thomas, Phys. Rev. Lett. 92, 162501 (2004).

[3] T. Otsuka, T. Suzuki, R. Fujimoto, H. Grawe and Y. Akaishi, Phys. Rev. Lett. 95, 232502 (2005).

[4] M.S. Fayache, L. Zamick and B. Castel, Physics Reports 290, 201 (1997).

[5] T. Otsuka, T. Matsuo and D. Abe, Phys. Rev. Lett. 97, 162501 (2006).

[6] B.A. Brown, T. Duguet, T. Otsuka, D. Abe and T .Suzuki, Phys. Rev. C 74, 061303 (2006).

[7] G. Colò, H. Sagawa, S. Fracasso and P.F. Bortignon, Phys. Lett. B 646, 227 (2007).

[8] G. Bassani and J. Picard, Nucl. Phys. A131, 653 (1969).

[9] E.R. Flynn, R.E. Brown, F. Ajzenberg-Selove and J.A. Cizewski, Phys. Rev. C28, 575 (1983).

[10] K.S. Low and T. Tamura, Phys. Rev. C11, 789 (1975).

[11] W.C. Parkinson, D.L. Hendrie, H.H. Duhm, J. Mahoney, J. Saundinos and G.R. Satchler, Phys. Rev. 178, 1976 (1969); Erratum Phys. Rev. 187, 1744 (1969).

[12] M.H. Macfarlane and Steven C. Pieper, Argonne National Laboratory Internal Report ANL-76-11 Rev 1, 1976, (unpublished).

[13] T.W. Burrows, Nuclear Data Sheets 92, 623 (2001).

[14] J.K Tuli and D.F. Winchell, Nuclear Data Sheets 92, 277 (2001).

[15] J.K Tuli, Nuclear Data Sheets 94, 605 (2001).

[16] J.K Tuli, Nuclear Data Sheets 86, 285 (1999).

[17] K. Heyde, M. Waroquier and H. Vincx, Phys. Letts. B 57, 429 (1975).

[18] L. Trache, A. Clauberg, C. Wesselborg, P. von Brentano, J. Wrzesinski, R. Broda, A. Berinde and V. E. Iacob, Phys. Rev. C 40, 1006 (1989).

[19] W. Booth, S. Wilson and S.S. Ipson, Nucl. Phys. A229, 61 (1974).

[20] A.M. Oros, L. Trache, P. von Brentano, K. Heyde and G. Graw, Phys. Scr. T56, 292 (1995).

[21] B.H. Wildenthal, E. Newman and R.L. Auble, Phys. Rev. C3, 1199 (1971).

[22] T. Otsuka, private communication (2007).

FIG. 1: Spectra from the (α,^{3}He) reaction as a function of excitation energy taken at 20° in the laboratory frame, labelled by residual nucleus. Peaks are labelled with the ℓ transfer of the transition. The large peak moving up through the spectra with increasing atomic number is due to reactions carbon and oxygen contaminants in the target. Small, broader peaks, particularly evident in the ^{145}Sm spectrum, arise from silicon contamination.

FIG. 2: Differential cross sections from the ^{144}Sm(α,^{3}He)^{145}Sm reaction shown for transitions leading to the following states in the residual system: (a) $13/2^+$ state at 1105 keV, (b) $9/2^-$ state at 1423 keV, (c) $13/2^+$ state at 2670 keV and (d) $9/2^-$ state at 1780 keV. Square points indicate $\ell = 5$ transitions, circular points $\ell = 6$ assignments. The lines are DWBA calculations normalised to the data, for ℓ=5 (continuous line) and for ℓ=6 (dashed line).

TABLE I: Optical-model and bound-state potentials used in the DWBA calculations. Depths of the bound-state potentials, marked with $\star$, were varied to reproduce the appropriate binding energies.

Channel	V MeV	r_r fm	a_r fm	W MeV	r_i fm	a_i fm	V_{so} MeV	r_{so} fm	a_{so} fm	Reference
^{4}He	207.0	1.3	0.65	28.0	1.3	0.52	–	–	–	[8]
^{3}He	152.0	1.24	0.685	23.0	1.432	0.870	–	–	–	[9]
N=82+n	$\star$	1.25	0.63	–	–	–	7.0	1.10	0.50	[11]
^{3}He+n	$\star$	1.20	0.65	–	–	–	–	–	–	[10]

FIG. 3: (a) Experimental centroid energies of the neutron $h_{9/2}$ single-particle strength for $N = 83$ nuclei (solid squares) compared to the quadrupole vibrational excitation energies of the corresponding even-even core (open symbols). (b) A similar plot for the $i_{13/2}$ centroid and octupole vibrations of the core. The difference in experimental centroid energies of $\nu i_{13/2}$ and $\nu h_{9/2}$ strength (solid triangles) compared to: (c) the energy differences between the lowest $13/2^+$ and $9/2^-$ states (open triangles), and (d) predictions of a $\pi + \rho$ tensor interaction (grey band). The width of the grey band is generated by experimental uncertainty in the proton occupancies [21].

TABLE II: Differential cross sections and spectroscopic factors of states populated by large ℓ transfer in the (α,^{3}He) reaction on stable N=82 targets. Excitation energies are taken from Ref. [13, 14, 15, 16].

	Excitation Energy (keV)	ℓ	Cross Section (mb/sr) 6°	11°	20°	30°	C^2S
^{139}Ba	1283.32(3)	5	–	–	0.35	0.20	0.70
	1538.96(11)	6	–	–	0.75	0.44	0.60
	1619(10)	5	–	–	0.18	0.11	0.41
	3080(10)	6	0.27	0.21	0.12	0.08	0.17
^{141}Ce	1354.52(9)	5	–	–	0.54	0.21	0.67
	1368.7(2)	6	–	–	1.01	0.57	0.79
	1693.3(1)	5	–	0.15	0.13	0.08	0.25
	2899(2)	6	0.44	0.31	–	0.15	0.22
^{143}Nd	1228.04(8)	6	2.68	2.06	1.19	–	0.65
	1407.08(6)	5	1.11	0.76	0.54	–	0.83
	1739.21(8)	5	0.34	0.22	0.16	–	0.29
	2805.3(3)	6	–	–	0.26	–	0.22
^{145}Sm	1105.3(16)	6	2.99	2.30	1.25	–	0.66
	1423.24(3)	5	1.18	0.87	0.62	–	0.84
	1780.32(9)	5	0.41	0.29	0.22	–	0.34
	2670.0(11)	6	0.87	0.62	0.41	–	0.30

TABLE III: Summed single-neutron strengths, energy centroids and mixing matrix elements with the state of corresponding j^{π} formed by coupling the $\nu f_{7/2}$ state to the 2^{+} or 3^{-} core vibrations.

	^{139}Ba		^{141}Ce		^{143}Nd		^{145}Sm	
	$h_{9/2}$	$i_{13/2}$	$h_{9/2}$	$i_{13/2}$	$h_{9/2}$	$i_{13/2}$	$h_{9/2}$	$i_{13/2}$
$\sum C^2S$	1.11(16)	0.77(11)	0.92(13)	1.01(14)	1.12(16)	0.87(12)	1.18(17)	0.96(14)
Centroid Energy (keV)	1407(10)	1879(24)	1447(10)	1702(52)	1493(5)	1627(31)	1526(10)	1594(29)
% Upper State	37(2)	22(1)	27(3)	22(3)	26(1)	25(2)	29(3)	31(1)
Matrix Element (keV)	162(6)	639(17)	151(5)	632(34)	145(2)	686(16)	162(4)	725(9)

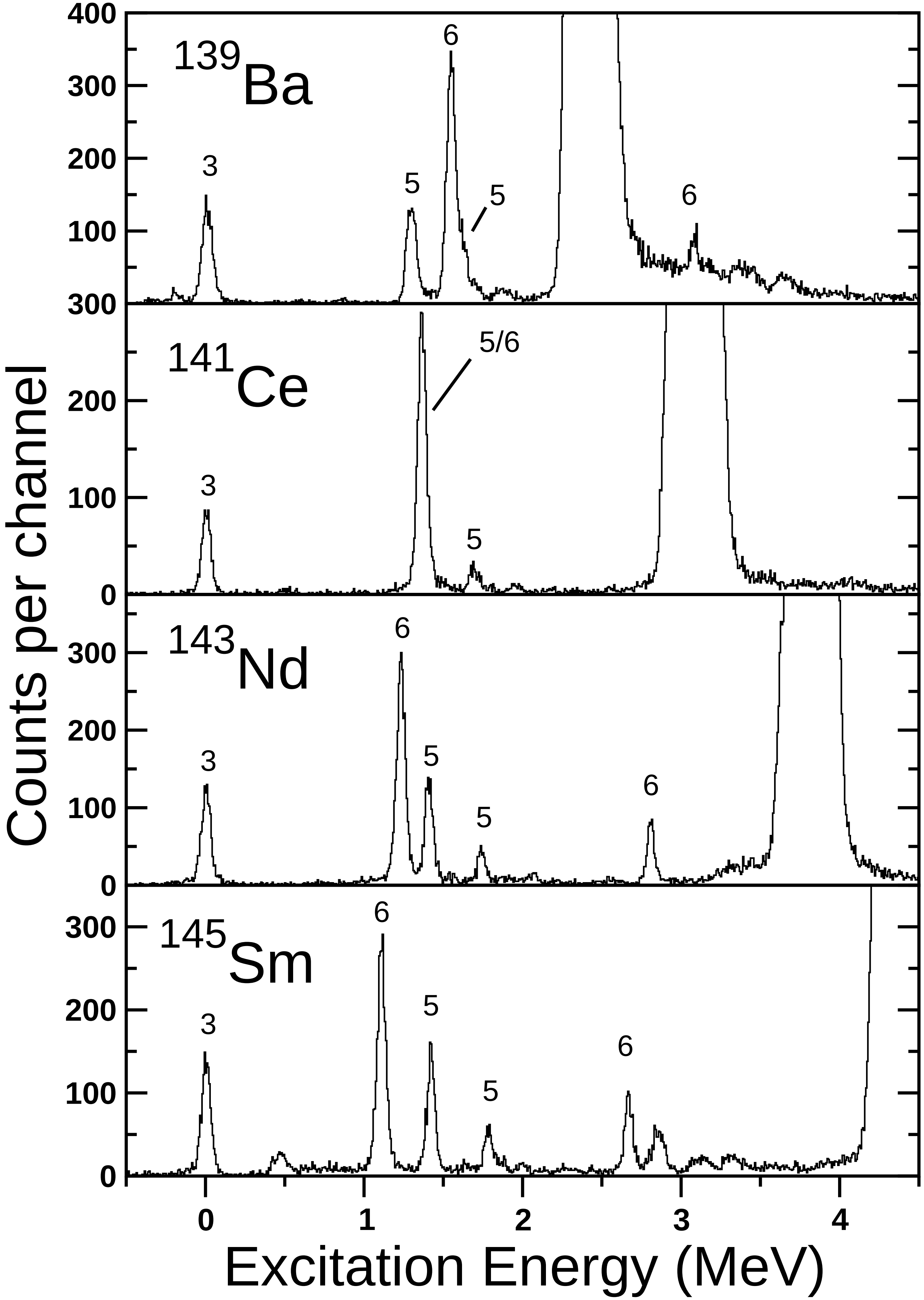
400
300
200
100
300
^{139}Ba
3
5
6
5
6
200
100
0
^{141}Ce
3
5/6
5
300
200
100
0
^{143}Nd
3
6
5
5
6
300
200
100
0
^{145}Sm
3
6
5
5
6
Counts per channel
0
1
2
3
4
Excitation Energy (MeV)

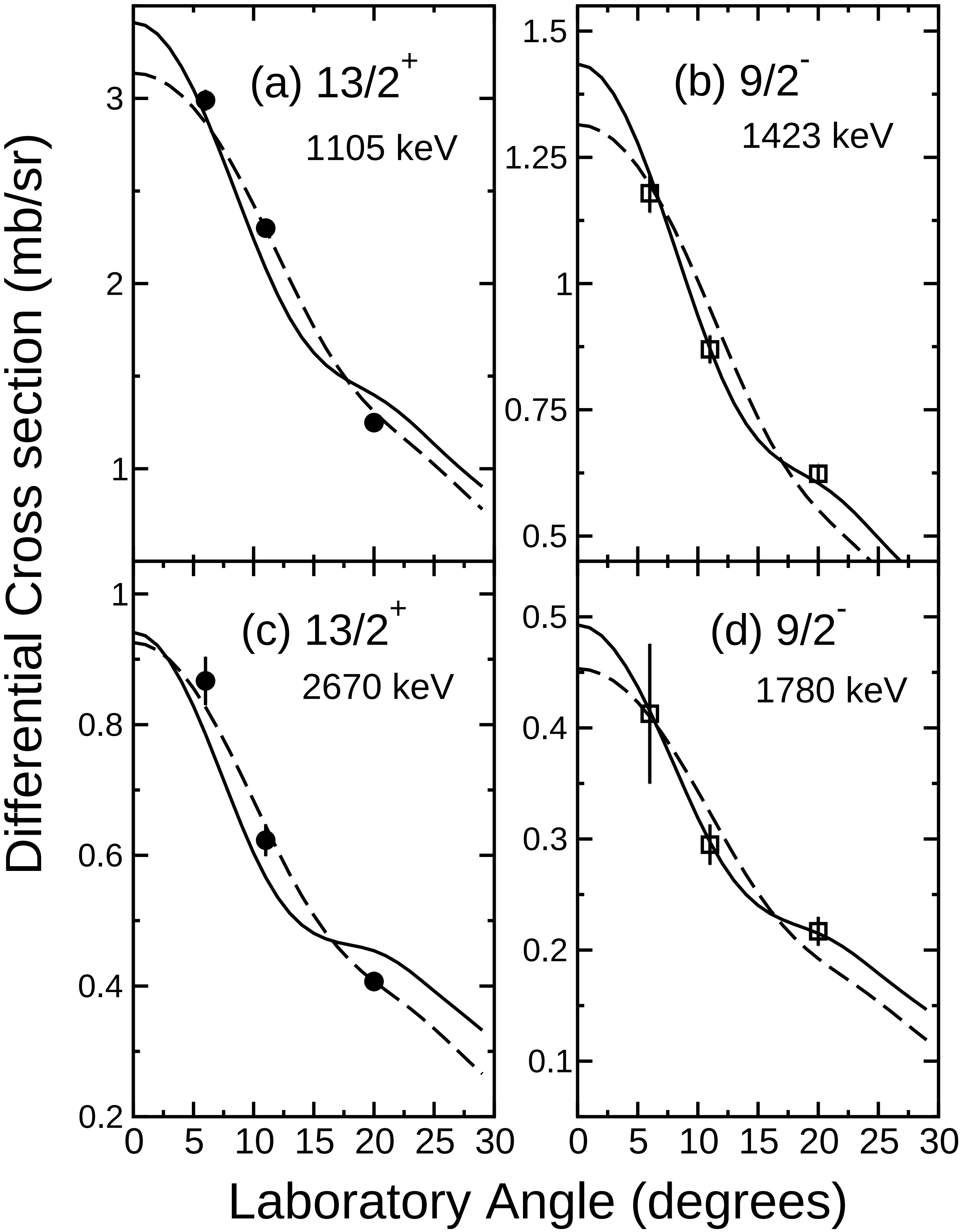
Differential Cross section (mb/sr)
Laboratory Angle (degrees)
(a) $13/2^+$
1105 keV
(b) $9/2^-$
1423 keV
(c) $13/2^+$
2670 keV
(d) $9/2^-$
1780 keV
3
2
1
1.5
1.25
1
0.75
0.5
1
0.8
0.6
0.4
0.2
0.5
0.4
0.3
0.2
0.1
0
5
10
15
20
25
30

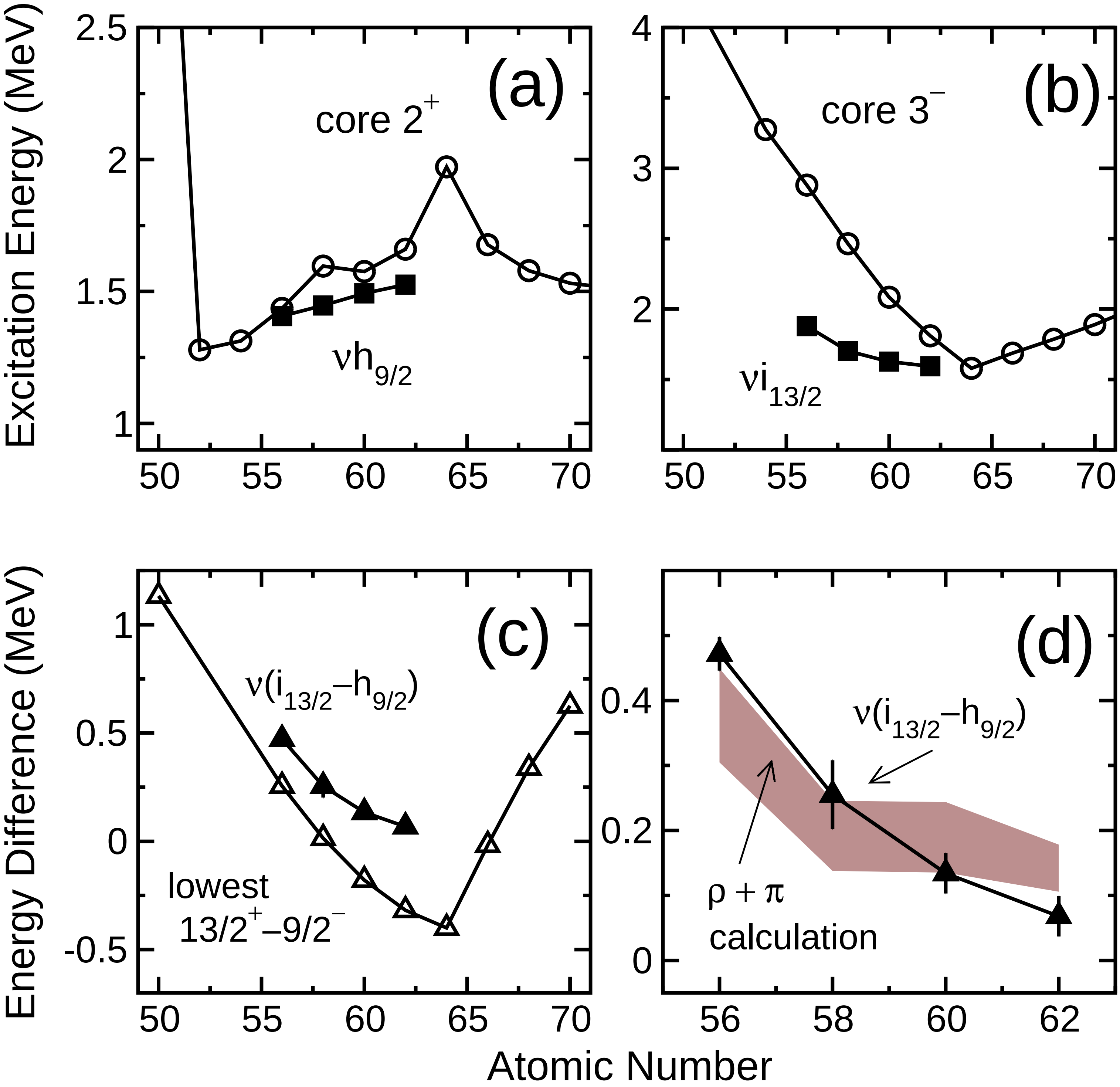

Excitation Energy (MeV)
Energy Difference (MeV)
Atomic Number
(a)
core 2^+
$\nu h_{9/2}$
(b)
core 3^-
$\nu i_{13/2}$
(c)
$\nu(i_{13/2}-h_{9/2})$
lowest
$13/2^+-9/2^-$
(d)
$\nu(i_{13/2}-h_{9/2})$
$\rho + \pi$
calculation
2.5
2
1.5
1
4
3
2
1
0.5
0
-0.5
0.4
0.2
0
50
55
60
65
70
56
58
60
62